

AN EXPERIMENTAL AND NUMERICAL ANALYSIS OF RESIDUAL STRESSES IN A TIG WELDMENT OF SINGLE CRYSTAL NICKEL-BASED SUPERALLOY

Jingwei Chen, Enrico Salvati, Fatih Uzun, Chrysanthi Papadaki, Zifan Wang, Joris Everaerts,

Alexander M. Korsunsky *

MBLEM, Department of Engineering Science, University of Oxford, Parks Road, Oxford OX1 3PJ, United Kingdom

alexander.korsunsky@eng.ox.ac.uk, *corresponding author

ABSTRACT

The Tungsten Inert Gas (TIG) welding technique is extensively used to join various automobile and aerospace components, such as control arms, rotating blades, and vanes. Highly localized heating followed by rapid cooling during welding exert complex thermal and mechanical loading on the components and give rise to significant residual stress fields which may increase the likelihood of time-dependent failure by promoting crack initiation. In the context of engineering design for structural integrity and reliability of operation, quantitative residual stress evaluation in the finished parts needs to be carried out in a reproducible manner. Samples investigated in this study were TIG fill-in weldments in single crystal superalloy components with nearly cylindrical geometry. The

present research employed Focused Ion Beam – Digital Image Correlation (FIB-DIC) micro-ring-core technique for stress evaluation, and a sequentially coupled thermo-mechanical finite element model to assess the residual stress state near the weldment surface in the radial and hoop directions. Good agreement was obtained between experimentally evaluated residual stresses and the refined numerically predictions. The highest hoop and radial tensile residual stresses were both observed near the boundary between the filler metal and base metal, whilst a compressive region was found for hoop stress in the parent metal at the component edge. These observations were discussed in conjunction with the temperature history and residual stress self-equilibration. This research provides the foundation for further investigations of Post Weld Heat Treatment (PWHT) and surface treatment to improve fatigue performance of weldments.

Keywords: Tungsten inert gas welding; Residual stress; Focused Ion Beam – Digital Image Correlation; Thermal-structural coupled analysis

NOMENCLATURE

σ_{xx}	Residual stress in the x direction
σ_{yy}	Residual stress in the y direction
e_{xx}	Relief strain in the x direction
e_{yy}	Relief strain in the y direction
σ_{rr}	Radial stress
$\sigma_{\theta\theta}$	Hoop stress
E	Young's modulus
ν	Poisson's ratio

1. Introduction

When gas turbine engines operate in service conditions, they experience extremely aggressive thermo-mechanical loading. In order to meet the demand for increased gas turbine performance, high-performance alloys are being developed to withstand higher stresses at working temperatures. Nickel-based superalloys are extensively used in manufacturing gas turbine blades and vanes for several decades due to their high-temperature strength and excellent oxidation resistance [1]. Traditionally, gas turbine engine manufacturers used polycrystalline nickel superalloys to fabricate turbine blades. However, these polycrystalline superalloys have relatively lower operating temperature compared to highly demanding turbine engines, in which a much higher turbine inlet temperature is required to increase the efficiency of gas turbine engines. In comparison with conventionally cast polycrystalline superalloys, single crystal nickel-based superalloys exhibit increased strength and creep resistance at a higher temperature and, accordingly, are increasingly used in turbine blade and vane fabrication [2].

The stress in gas engines varies during a typical flight cycle which includes taking off, cruising and landing stages. The temperature profile and stress states that accompany this loading are complex and non-proportional, so that both high stress/high temperature and high stress/low temperature combinations are encountered. The complex combination of creep and fatigue represents the most prominent damage mode. Furtado and Le May reported that superalloys will experience deterioration processes under creep and fatigue loading at high temperatures, and the degradation effects are enhanced by residual stresses [3], especially at the micro-scale (Type II and III residual stress [4]).

Consequently, investigating the residual stresses at appropriate scales is critical for understanding the operating conditions of these superalloys, as it allows the development of improved design methods for enhanced structural integrity.

TIG welding is a bonding technique extensively used to join various automobile and aerospace components. It uses a non-consumable tungsten electrode that delivers the current to the welding arc. The electrode and weld area are protected from oxidation and cooled with an inert gas, typically argon or helium, and filler metal is normally used. Residual stress is that which presents within the material body without external loading and is self-balanced with its surroundings [5]. It can be introduced into engineering components during manufacture e.g., forging, bending and welding processes, as a result of forces and thermal loading history. The highly localized temperature profile around the weld zone will cause considerable welding residual stress and possibly, deformation [6]. The presence of residual stresses can increase the likelihood of time-dependent failure by acting as a driving force for crack initiation. To optimize the weld manufacturing process and quantify the effect of welding residual stresses on nickel superalloys performance, it is necessary to research their magnitude and distribution [7].

The residual stress evaluation techniques can be classified into two principal approaches: non-destructive, such as Electron Backscattered Diffraction (EBSD) and X-ray diffraction, and destructive or semi-destructive (minimally disturbing) methods based on material removal and strain relief measurement [8]. In terms of crystalline materials, X-ray or neutron-based diffraction and EBSD

method are widely used to measure residual stress. X-ray diffraction is one of the most powerful residual stress analysis methods that can achieve sub-micron resolution with the help of synchrotron X-ray beams. However, there are mainly two limitations to this synchrotron-based method. One is that access to synchrotron instruments is restricted, the other is that this technique is limited to crystalline materials with high perfection and the X-ray transmission depth is relatively small [9]. EBSD technique can enable sub-micron measurement of residual stress by the examination of Kikuchi patterns. Nevertheless, it is normally confined to free-surface measurement and is rather time-consuming and expensive [10-14]. It is important to note that stress-free lattice parameters of the materials must be first investigated to calculate the residual stress for both XRD and EBSD based methods.

Another promising residual stress measurement method is the recently developed FIB-DIC micro-ring-core milling technique. This semi-destructive method is based on the measurement of localized strain relief through core milling [15]. FIB is employed to mill incrementally a circular trench or micropillar in the material surface. A contrast pattern is deposited by Pt or Au on the micropillar top surface. It is then possible to measure the strain relief using DIC software in successive SEM images [16]. Finite element simulation shows that the residual stress is completely relieved when the micropillar depth becomes comparable with its diameter [17]. Accordingly, together with the knowledge of material elastic properties, the pre-existing local residual stress can be reconstructed from the strain relief [8]. In principle, with the help of FIB-DIC and eigenstrain modelling, macroscopic (Type I) and microscopic (Type II+III) residual stresses can be separated [4,18]. In

comparison to other non-destructive through thickness averaging methods (e.g. neutron and synchrotron X-ray diffraction techniques), FIB-DIC method does not require the knowledge of stress-free lattice parameters, thus providing absolute residual stress value [18]. In addition, the gauge volume, which is determined by the diameter and depth of micropillar, is more precisely defined in FIB-DIC. In the last decade, FIB-DIC method has been well developed on account of increasing accessibility of SEM and FIB systems, as well as improved DIC software [9]. Therefore, FIB-DIC has become increasingly popular and affordable for small and medium-sized facilities to obtain efficient residual stress evaluations.

In the present paper, FIB-DIC micro-ring-core milling technique and finite element modelling are both employed to assess the residual stress state near a weldment surface along radial and hoop directions. Manual TIG welding is performed on sample components to fill in a hole by filler metal (Ni alloy). The residual stress in the as-welded sample was evaluated by FIB-DIC, followed by simulation of stress distribution by a coupled thermo-mechanical Finite Element Method (FEM) model using ABAQUS. Finally, experimental evaluation and thermal stress simulation results are compared to confirm that a good agreement is achieved.

2. Specimen and microstructure

2.1 Material and specimen

The as-welded specimens were provided by Rolls-Royce plc. The base material used was a single

crystal nickel superalloy CMSX-4. It is a second-generation high strength single crystal superalloy designed for small gas turbine engines [19]. The solid solution strengthening elements include Rhenium, Chromium, Tungsten, and Tantalum. The addition of Titanium and Aluminum provides further precipitation hardening effect since they are γ' phase stabilizer [20]. The composition of CMSX-4 in this study is shown in Table 1. The central hole of the specimen was filled with Polymet 972 welding wire manufactured by Polymet Corporation. The composition of the welding wire is given in Table 2.

Table 1. The chemical composition of the CMSX-4 used in this specimen.

Element content, wt.%								
Cr	Co	Mo	Al	Ti	Ta	Hf	Re	Ni
6.5	9.0	0.6	5.6	1.0	6.5	0.1	3.0	Bal.

Table 2. The chemical composition of the Polymet 972 welding wire.

Element content, wt.%								
Ni	Co	Cr	W	Al	Ta	Ti	C	Other
15	Bal.	20	9	4.4	3	0.2	0.35	1.5

The geometry of the weldment is complex. It is possible to identify the region of parent metal (single crystal CMSX-4) unaffected by welding; the filler metal forming a lozenge-shaped ‘plug’ that is approximate 3 mm high and 5 mm in diameter, and the fusion and Heat Affected Zone (HAZ) between

them. Fig. 1 illustrates the weld geometry, and a cross-section view through the weldment. The welded hole is indicated by two red arrows. Radial and hoop direction are defined using polar coordinate system (show in Fig.1) at an arbitrary angle α . In this research, α was chosen to be 0° during experimental residual stress evaluation in order to simplify the stress analysis. The real geometry of the substrate is represented by a cylinder of 7mm thickness with a central hole approximately 6mm in diameter. A fill-in weldment was considered that blocked the through-hole present at the center of the sample before welding. It is apparent from Fig. 1 that there exists a hollow area below the filler metal after welding.

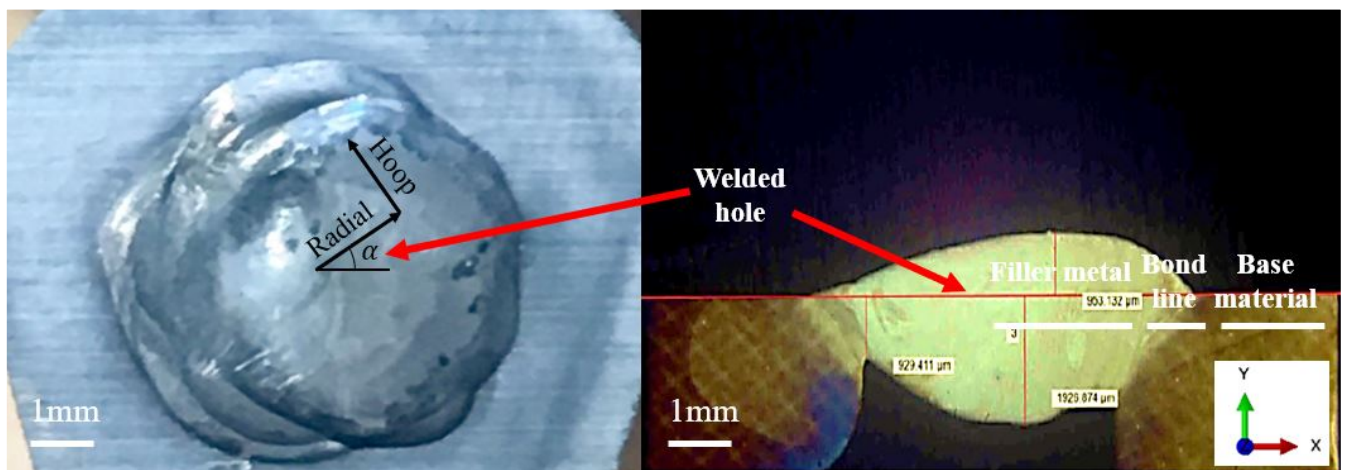


Figure 1. The overall geometry of the welded specimen with arrows showing the weld infill (left), and a cross-section view through the weldment (right).

The weldment was sectioned to give an indication of the size of HAZ. The minimum HAZ thickness was 0.44mm, and maximum depth was 2.26 mm. No welds showed any distortion or cracking. The top bead of the welding area was removed by standard metallographic grinding, followed by

mechanical polishing in a solution containing a suspension of 9 μm , 3 μm and 1 μm diamond particles. The top surface was then electrochemically polished at room temperature with a current density of 0.005 A/mm². The electrolyte used contained absolute methanol with 20% vol. sulphuric acid [21]. No further residual stress was introduced by this surface preparation process [22]. The sample height was measured in as-received condition and after polishing, and it was found that materials 0.95 mm below the surface of base metal was machined away during grinding and polishing process.

2.2 Microstructure and texture analysis

Prior to FIB milling, secondary electron (SE) detector was used to examine the microstructure of welding surface. The accelerating voltage for all SEM images was 10 kV. The microstructure of the as-welded specimen is shown in Fig. 2. The interface between welding metal and base metal can be clearly distinguished from the secondary electron image in Fig. 2 (a) and (b). The left region with a coarse surface in Fig. 2(b) is unaffected base metal CMSX-4, while the right is welding metal Polymet 972. A closer observation of base metal (Fig. 2(c)), which illustrates the microstructure of single crystal, shows gamma prime phase with very fine secondary gamma prime precipitates in between.

As the sample is nearly axisymmetric, EBSD orientation mapping was performed on a quarter of the specimen, containing a filler metal zone, the bond line, and the base metal. The inverse pole figure in Fig. 3 illustrates the grain morphology and orientations in the one-quarter specimen. A clear boundary between the base metal and filler metal is shown since the unaffected base metal is a single crystal nickel superalloy, while the grain size and orientations vary in filler metal. The single crystal

orientation was fully determined in terms of the Euler angles, which were 77.4° , 31.9° , and 0.8° in the Bunge notation. The grains in fusion zone are narrow and highly elongated in the radial direction with respect to the sample center. This shape is formed because of the steep temperature gradient during welding process in the radial direction. The single crystal can be seen as a seed for grains near it, consequently, many grains at the interface exhibit the same orientation as the single crystal superalloy. Since the elongated grains have dimensions that range between 50 and 800 μm in the radial direction that are larger than the diameter of the FIB milling rings (see Fig.5), the residual stresses evaluated by FIB-DIC represent the full grain level Type I+II+III residual stress.

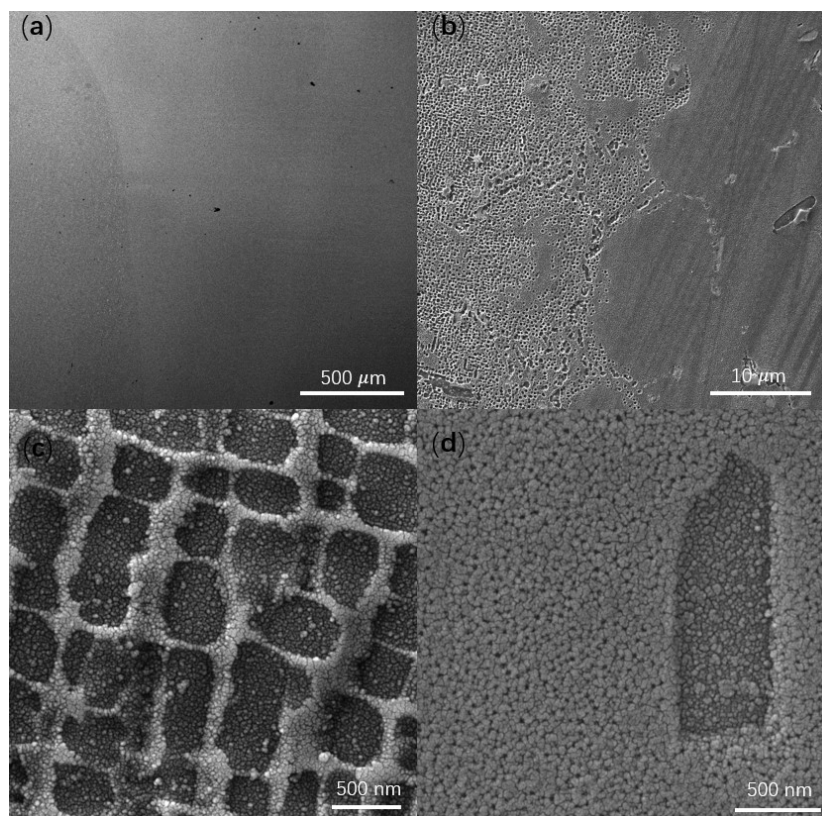


Figure 2. Secondary electron images showing the microstructure of the welded specimen at different locations:

(a) The interface between welding metal Polymet 972 and unaffected base metal CMSX-4. (b) A close-up image of the interface. (c) The microstructure of single crystal base metal. (d) The microstructure of welding area.

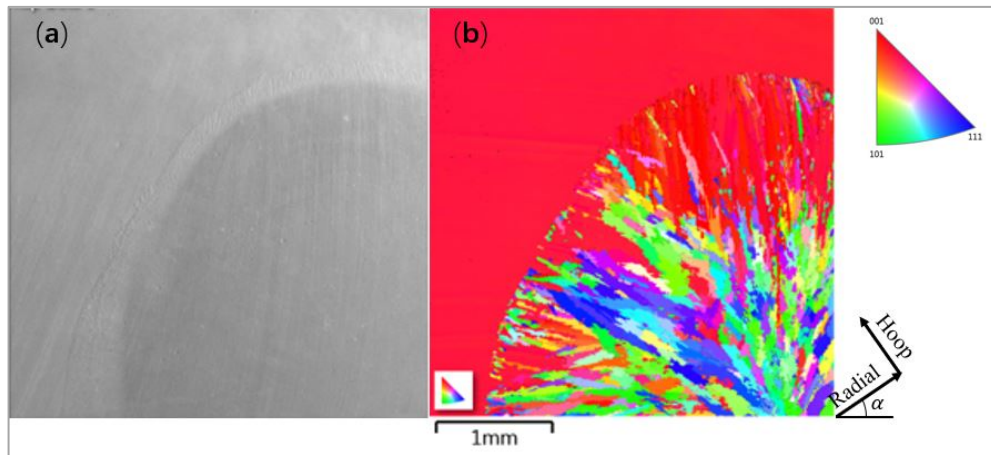


Figure 3. (a) SEM image showing the texture in analysis area. (b) Inverse pole figure map for a quarter of the sample (with respect to the hoop direction).

3. Residual stress evaluation and numerical simulation

3.1. FIB-DIC micro-ring-core milling for residual stress evaluation

All SEM imaging and FIB milling were performed using LYRA3 FIB-SEM system (Tescan, Czech Republic) at MBLEM lab, Oxford. The top surface of the specimen, along with FIB-DIC test positions, are illustrated in Fig 4. Grain morphology and orientation were investigated by EBSD using Oxford Instruments NordlysNano detector. Since the strain relief is quantitated by DIC analysis, reasonable contrast is required on the micropillar top surface in order to obtain accurate displacement measurements. Before FIB milling, a thin Pt layer (~5 nm) was deposited on the sample surface so that DIC displacement could be tracked precisely. The random distribution of Pt particles on the surface allowed reliable DIC post-processing. No additional stress was introduced by the deposition of this extremely thin and discontinuous layer [23].

The ion beam energy was set to 30 keV for milling. The inner diameter of micropillar was chosen to be 20 μm , with a 2 μm trench width. The micro-ring-core milling process was performed in 60 steps, providing a total depth of 7 μm . After each milling step, 10 successive SEM images were recorded with short dwell time. The displacement of markers containing 12 pixels was calculated, and then the relieved strain changed with milling depth in x and y directions were determined. The averaging of 10 images minimized the influence of SEM imaging artefacts during the DIC strain analysis. Finally, the obtained displacement field was fitted with a numerical master function to get the in-plane relief strain components [8]. Based on Hooke's law, the residual stresses in x and y directions were then determined. The above measurement approach provided average values of residual stress within a gauge volume, which is 20 μm in diameter and 7 μm in depth.

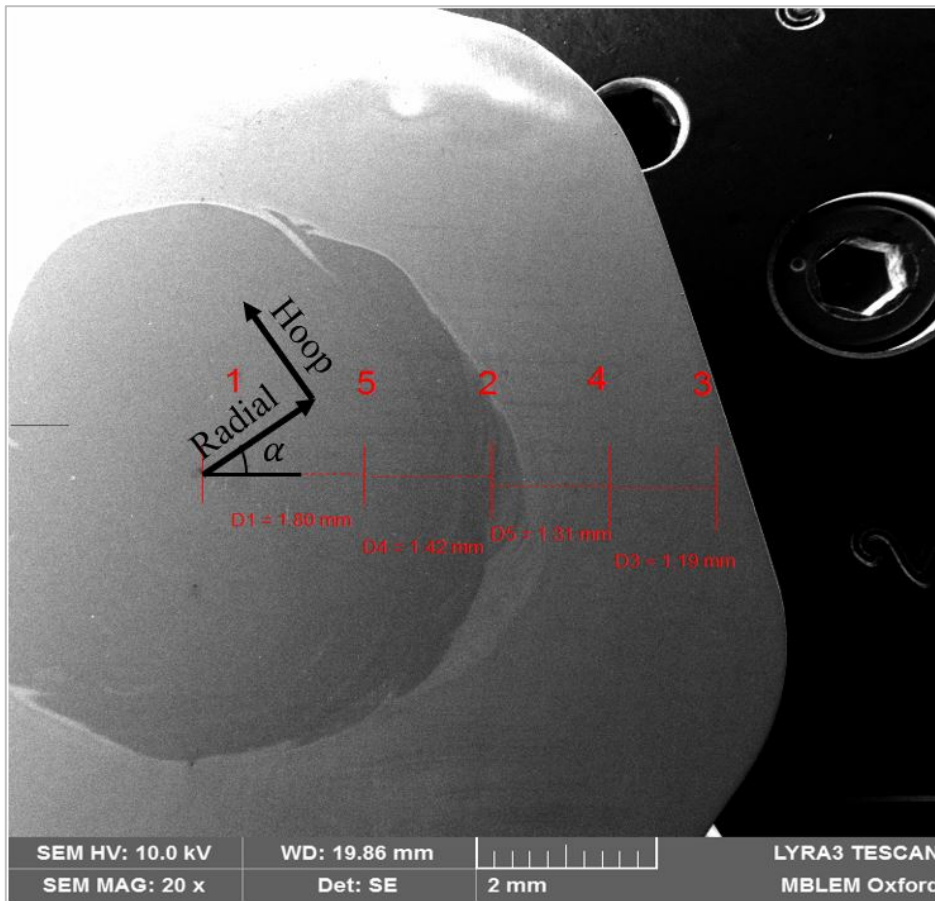


Figure 4. The FIB-DIC measurement positions in the sample surface.

In total, FIB-DIC residual stress measurements were performed at 5 and 8 different locations from the sample center to edge along the radial direction in two samples, respectively. The average distance between these test locations was ~ 1.35 mm. At each measurement point, 60 incremental milling steps were used, with 10 images taken at each step, providing a sequence of 600 images. The material removal process and the SEM images acquired are illustrated in Fig. 5 (a). These images were processed using a MATLAB-based DIC software [15], and data from 10 images for each milling increment was averaged. This was followed by a data refinement procedure to detect and remove any outliers. Fig. 5 (b) shows the strain relief curves in the radial (e_{rr}) and hoop ($e_{\theta\theta}$) directions for one measurement location.

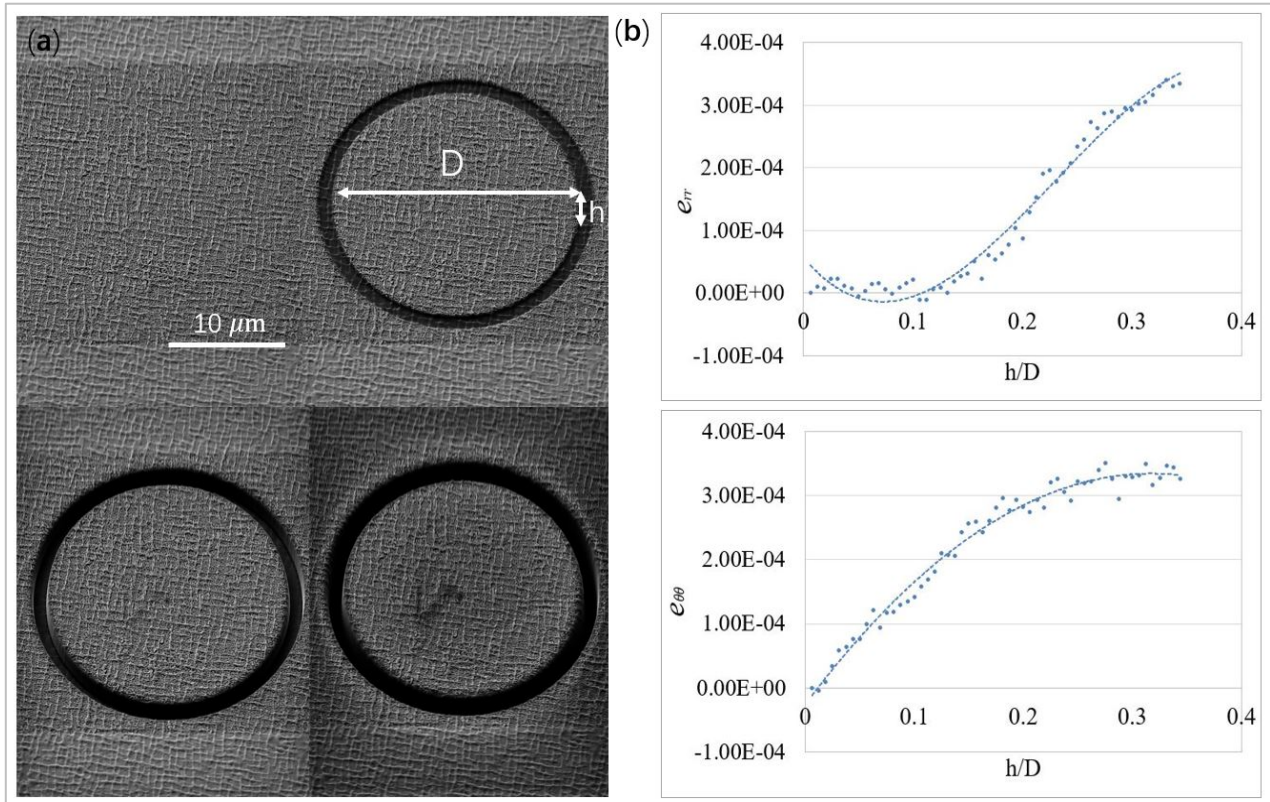


Figure 5. (a) An illustration of the FIB milling process. (b) A sample showing strain relief in two referent directions. D is the micropillar diameter and h is the milling depth.

For plane stress state, the residual stress profile was then been reconstructed for two orthogonal directions using Hooke's law. The residual stress in the x direction, σ_{xx} , and in the y direction, σ_{yy} can be evaluated from the following equations:

$$\sigma_{xx} = \frac{E}{(1 - \nu^2)} [\epsilon_{xx} + \nu \epsilon_{yy}] \quad (1)$$

$$\sigma_{yy} = \frac{E}{(1 - \nu^2)} [\epsilon_{yy} + \nu \epsilon_{xx}] \quad (2)$$

In the above equations, E is Young's modulus, ν is Poisson's ratio, and ϵ_{xx} and ϵ_{yy} are the components of residual elastic strain in the corresponding directions. It is worth noting that the strong

elastic anisotropy of cubic structure will introduce a further error in residual stress evaluation. The nickel-based superalloys are known to exhibit significantly high anisotropy, and the dimension of each micropillar is smaller than the grain size in both single crystal CMSX-4 and welded area. Accordingly, the crystallographic orientation of each grain within FIB-DIC measurements was considered based on the generalized Hooke's law. Instead of using average Young's modulus, Salvati et al. proposed to evaluate the anisotropic residual stress using the stiffness coefficient matrix calculated based on the Euler angles [24]. The following stiffness matrix was used when calculating residual stress:

$$\begin{pmatrix} \sigma_{11} \\ \sigma_{22} \\ \sigma_{33} \\ \tau_{23} \\ \tau_{31} \\ \tau_{12} \end{pmatrix} = \begin{pmatrix} C_{11} & C_{12} & C_{12} & 0 & 0 & 0 \\ C_{12} & C_{11} & C_{12} & 0 & 0 & 0 \\ C_{12} & C_{12} & C_{11} & 0 & 0 & 0 \\ 0 & 0 & 0 & C_{44} & 0 & 0 \\ 0 & 0 & 0 & 0 & C_{44} & 0 \\ 0 & 0 & 0 & 0 & 0 & C_{44} \end{pmatrix} \begin{pmatrix} \varepsilon_{11} \\ \varepsilon_{22} \\ \varepsilon_{33} \\ \gamma_{33} \\ \gamma_{31} \\ \gamma_{12} \end{pmatrix} \quad (3)$$

The elastic material properties used in the stress evaluation process are listed in Table 3 for both alloys. Fig. 6. shows the residual stress profile in two samples measured by FIB-DIC. The left sample had 8 measurement points, while the right one had 5 points. It is clear that the magnitude of residual stresses in these two samples was not exactly the same. However, the overall stress profile followed the same trend as the distance from center increases. The maximum tensile stresses (around 500-700 MPa) were both observed near the bond line. In the two specimens, stresses both decreased from the filler hole center to the bond line, followed by a sudden increase at the bond line. The stresses both

decreased from the bond line to the sample edge. In order to get a numerical description of such residual stress profile, in the next section, a thermal-structural coupled analysis was performed to simulate the residual stress after welding. And because the residual stress profiles in two samples are similar, only one sample (right) was chosen to compare the simulation results with experiment.

Table 3. The elastic properties for CMSX-4 and welding wire Polymet 972 at room temperature.

Material	C_{11} (GPa)	C_{12} (GPa)	C_{44} (GPa)	ν
CMSX-4	235.228	142.345	128.808	0.29
Polymet 972	334.852	164.927	84.962	0.33

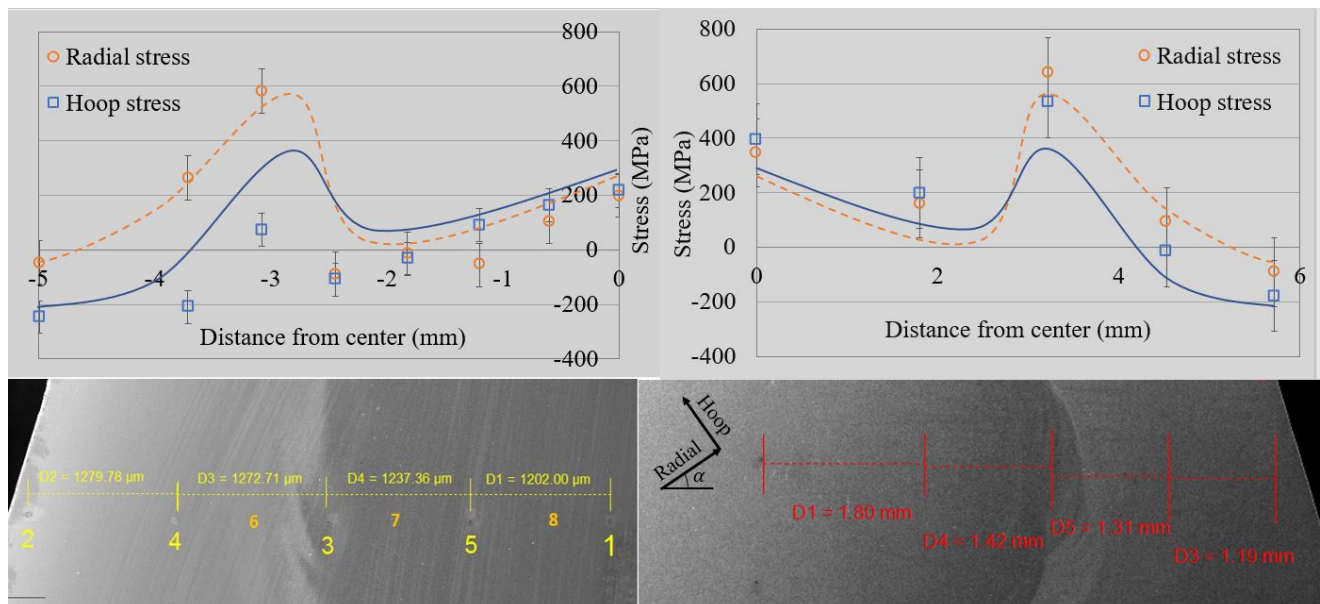


Figure 6. Radial stress (σ_{rr}) and hoop stress ($\sigma_{\theta\theta}$) obtained from FIB-DIC measurements with error bars at 95% confidence. The dash guideline curve shows the averaged radial stress with respect to distance from center, while solid line represents the trend of averaged hoop stress.

3.2. *FEM simulation*

Finite element modelling was performed for the manually welded specimen to calculate the residual stresses in hoop and radial directions using a commercial finite element software ABAQUS. A sequentially coupled thermo-mechanical analysis was introduced in this study. In the past years, many researchers have tried to simulate the distribution of heat flux during welding process. For instance, Gaussian heat source was used for simulating the temperature distribution during EDM cutting [25], or more specifically TIG welding process [26,27]. The body heat flow is distributed as Gaussian distribution from the tip of the electrode. In this paper, simplified Gaussian heat source was used to simulate the thermal history during welding, providing a temperature input for subsequent structural analysis.

Since the sample is approximately axisymmetric about its center line, therefore an axisymmetric model was employed to optimize the computational cost and results accuracy. Fig. 7 shows the detailed dimensions and mesh of the axisymmetric model. The model represents the material within the cross-section view shown in Fig. 7 (a). There is an apparent discrepancy in terms of the interface between filler metal and base metal for different samples. The interface line is not fully axisymmetric even in the same sample. Accordingly, interface sensitivity analysis was performed to evaluate how the residual stress profile changes due to interface geometry. Three interface lines (a, b, c in Fig. 7(b)) were built. Interface a and c indicate the inner and outer limit for the interface location, respectively, based on sample geometry measurement, while interface b is optimized to match the experimental residual stress profile in the current study. DCAX4 (4-node linear axisymmetric heat transfer

quadrilateral) elements were used from the ABAQUS element library [28] for the thermal model, while CAX4R (4-node bilinear axisymmetric quadrilateral, reduced integration) elements were applied in the subsequent mechanical model. Mesh size was determined through sensitivity analysis in this axisymmetric model. A refined mesh was generated within the filler metal and the bond line, where higher stress and larger stress gradient are expected.

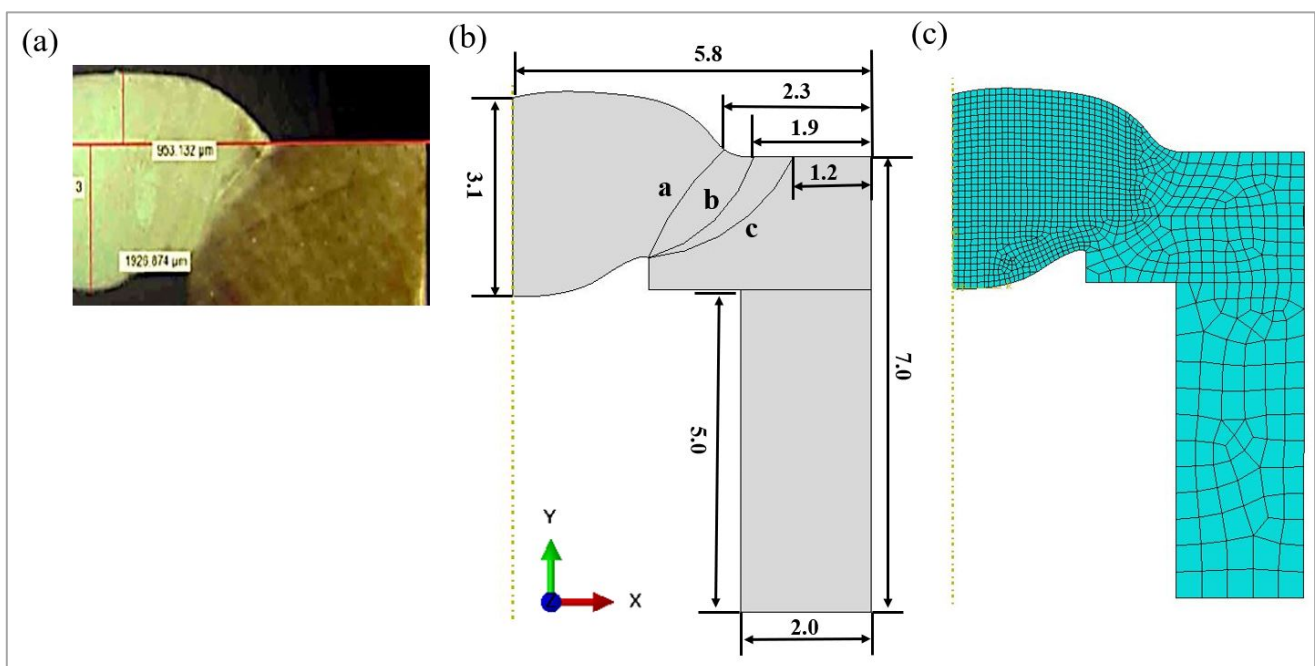


Figure 7. (a) The geometry of the sample. (b) The corresponding axisymmetric model with 3 different interface lines. (c) The refined mesh with interface b. The radial direction is along the x coordinate, while the hoop direction is perpendicular to the x-y plane.

Temperature-dependent mechanical properties, which is shown in Fig.8, were utilized for materials in different regions. Isotropic hardening and Von Mises yield criterion were employed in this simulation. The temperature dependent properties for CMSX-4 can be found in the literature [20, 29],

while for Polymet 972, the properties of a similar composition Co-Cr-Ni alloy (Elgiloy) [30, 31] were used in this simulation. Other thermal properties are listed in Table 4. Thermal and mechanical boundary conditions are illustrated in Fig. 9 (b). A thermal heat transfer model with Gaussian heat source was first simulated. Thermal conduction, convection and radiation were considered during the whole welding process. Thermal conduction was allowed between different zones. Convection and radiation with air were both considered at all the surface except the edge overlapped with axisymmetric axis, having coefficients of $24 \text{ mW}/(\text{mm}^2\text{K})$ and 0.8, respectively. Subsequently, the temperature history calculated by the thermal analysis was input as a predefined field for a mechanical model. Axisymmetric boundary condition was applied at the left edge of the model about y axis. The movement in y direction of the point at bottom right corner was constrained.

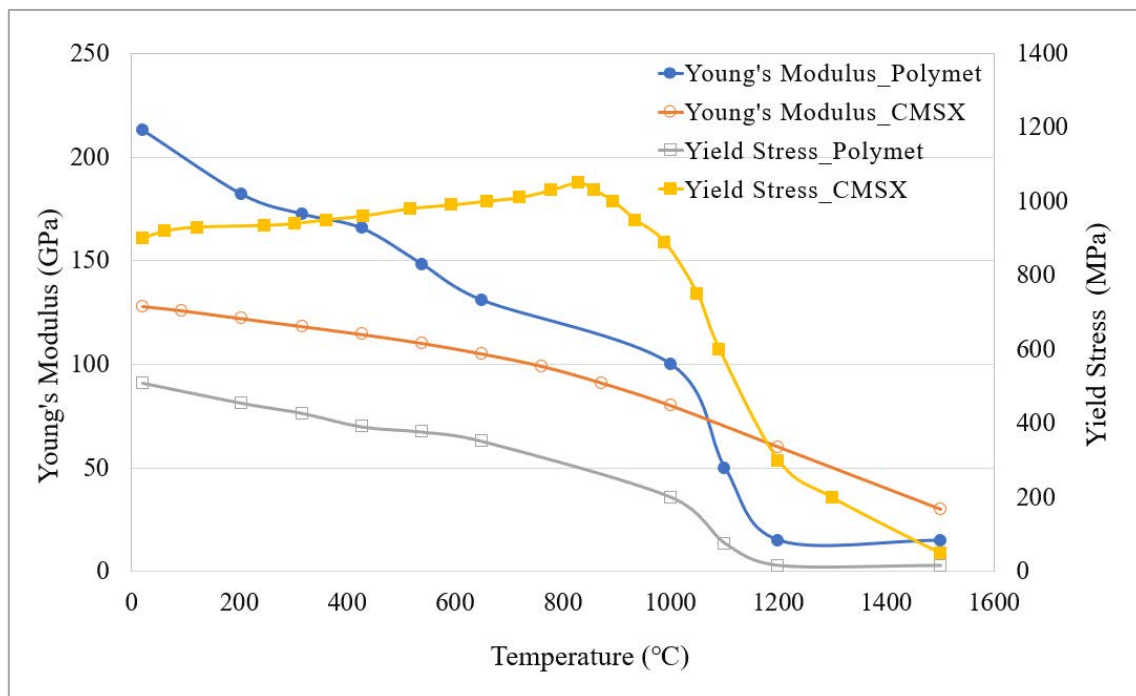


Figure 8. Temperature dependent mechanical properties.

Table 4. Other material properties used in the finite element model.

Properties	CMSX-4 single crystal	Polymet 972 welding wire
Density (Kg/m ³)	8.6E003	8.3E003
Coeff. Of Expansion (K ⁻¹)	1.28E-005	1.27E-005
Conductivity (W/m/K)	9	12
Specific Heat (J/T/K)	4.29E005	4.30E005

Based on the consideration of the process of infill welding, the principal operative heat source during welding moved in a spiral route from center to the bond line (see Fig. 9 (a)). This heating process can be simplified into 3 steps in the axisymmetric model. (1) Gaussian heat source was first applied in the model center and held for a period t_0 , (2) then the model was cooled for a short time t_1 , (3) after which the same heat source was applied near the bond line for t_2 (see Fig. 9 (b)). The whole model was subsequently cooled to room temperature. As the thermal history during welding was not provided by the manufacturer, trials were performed to find the optimal thermal parameters to achieve residual stresses that match with the experimental evaluation. Subsequently, the whole temperature history of heat transfer was input as a predefined field into the mechanical structural analysis.

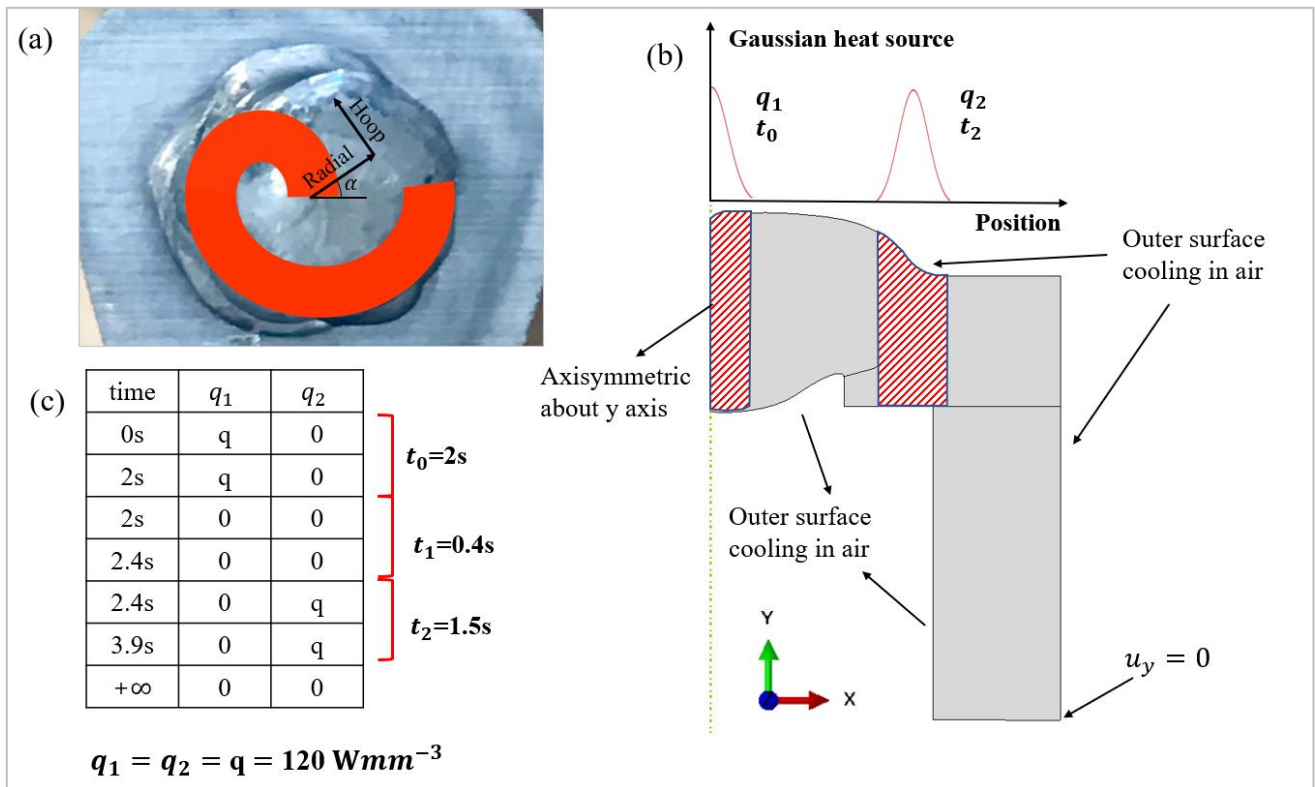


Figure 9. (a) The proposed route of heat source from the center to the edge. (b) An illustration of simplified heat source in axisymmetric model. (c) The heating parameters used in this simulation.

Fig. 10 is the contour diagram showing residual stress distribution across the model with optimized interface b right after welding. After thermal and mechanical simulation, the elements above the path A-B shown in Figure 10 were removed to reflect the effect of sample preparation by grinding and polishing before FIB-DIC stress evaluation. Therefore, this model was used to simulate both the welding process and material removal by grinding/polishing process. Fig. 11 illustrates the distribution of three components of residual stresses before and after material removal in the model with optimal interface b. It is clear that the maximum magnitude of radial, axial and hoop stress all drop approximately 200 MPa after polishing process. In addition, the axial stress in the top free surface becomes zero (shows in Fig. 11(d)) after material removal process, indicating that current

modelling result is reasonable. As FIB-DIC evaluates the residual stress at material surface, in order to make experimental stress evaluation comparable to simulation result, radial and hoop stress profile at the top free surface after cutting (shows in Fig.11(b) and (f) respectively) were obtained and plotted using red line with circular markers in Fig. 12. The residual stress profiles obtained from the other two models with interface a and c are also illustrated in Fig. 12. As can be seen in Fig. 12 that the magnitude of both radial and hoop stress, and the position of stress discontinuity change with different interfaces. However, the overall stress profile in all three cases followed the same trend as the distance from center increases. In this simulation, the inner and outer limit of interfaces (interface a and c) were first found based on the sample measurement, an optimized interface position (interface b) was then determined in between to match residual stress obtained from FIB-DIC evaluation. It is argued that in such way the residual stress can be accurately simulated without a full 3D description of interface.

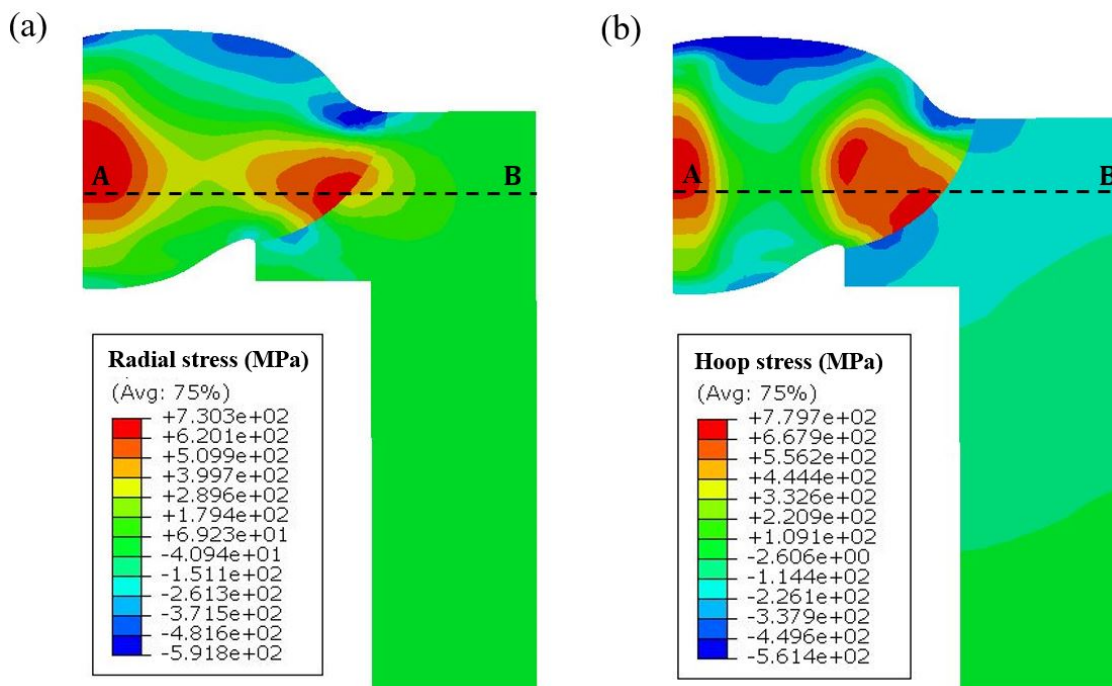
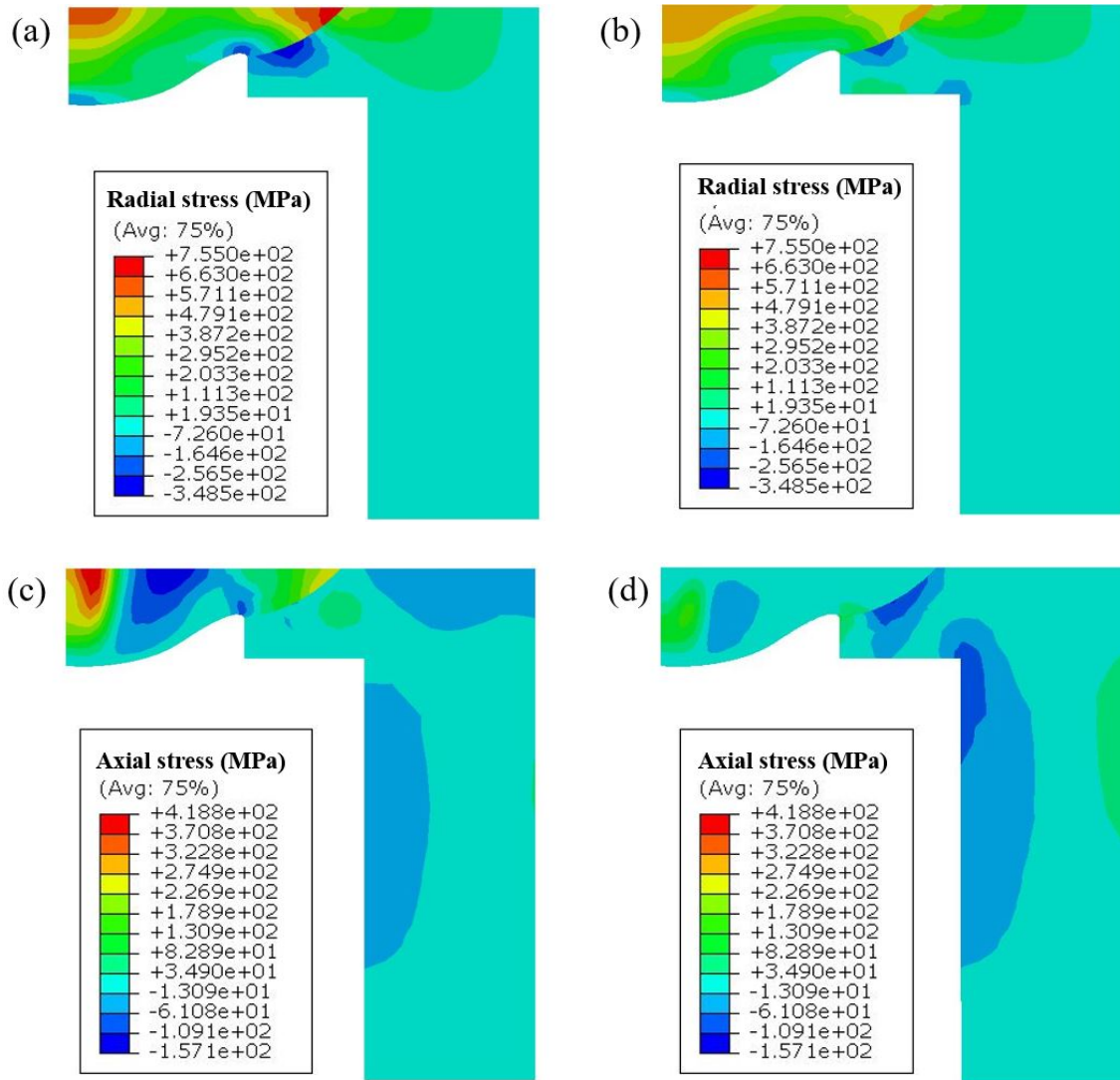


Figure 10. The distribution of radial stress (left) and hoop stress (right) right after welding in the model with optimal interface b.



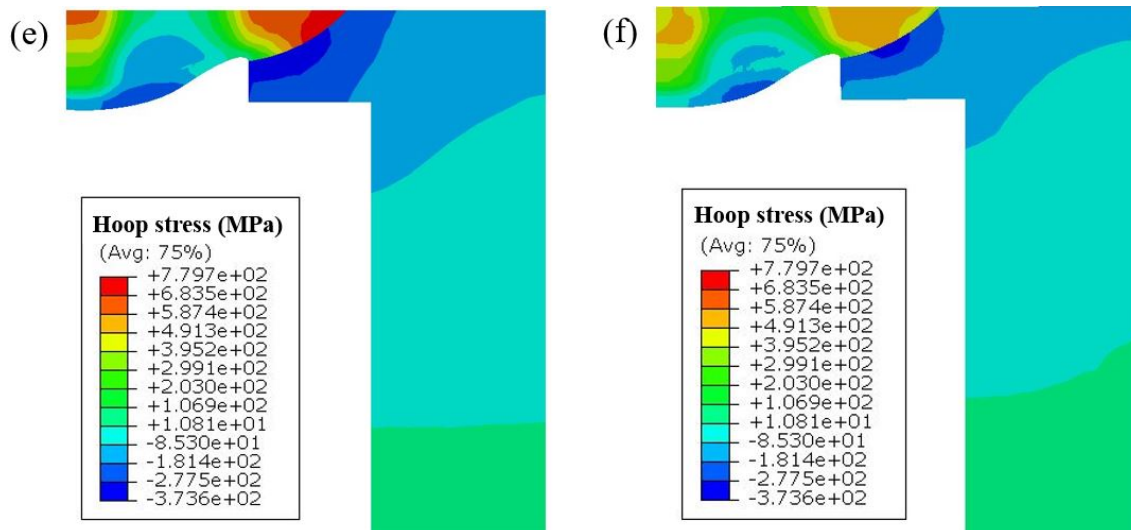


Figure 11. Three stress components distribution before ((a), (c), (e)) and after ((b), (d), (f)) material removal with optimal interface b.

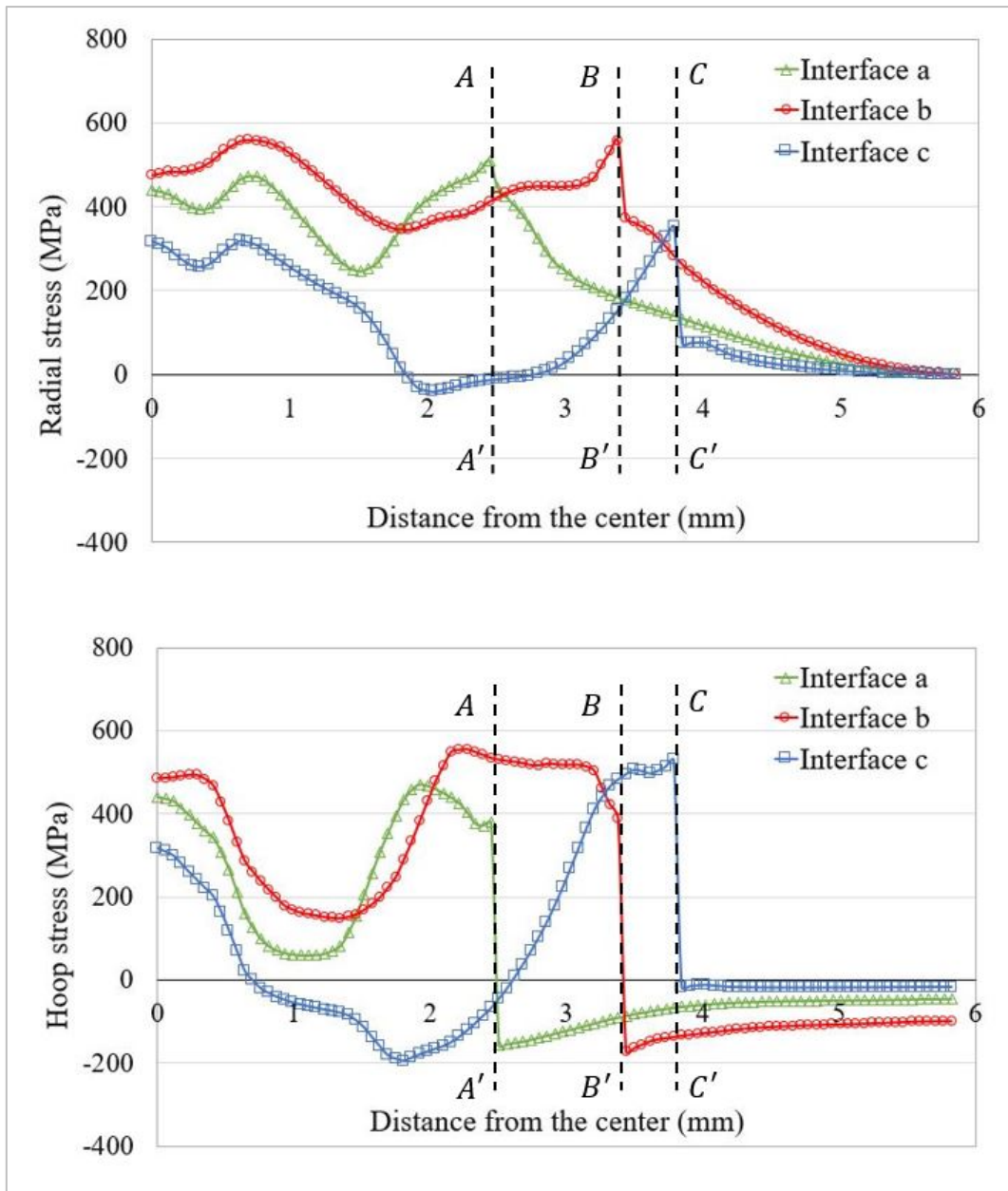


Figure 12. Radial (top) and hoop (bottom) residual stresses obtained from FEM near the top surface after cutting with three interfaces. Path $A-A'$, $B-B'$ and $C-C'$ indicate the position of interface a, b and c, respectively.

4. Result evaluation

4.1 Radial Residual Stresses

A stress acting parallel to the radius direction is known as a radial residual stress, denoted σ_{rr} in Fig. 6. Fig. 13 (a) depicts the distributions of the radial residual stress σ_{rr} in both FIB-DIC measurements and FE modelling with optimal interface b. The height of error bars is as much as 200 MPa, and almost all the FEM radial stresses are within the experimental error bar. Radial stress starts at around 450 MPa in the center, and then it drops slowly to 340 MPa. The largest tensile stress, which is approximately 570 MPa, is observed at the interface between the filler metal and base metal. This is followed by a decrease to zero as the distance from the center increases. On account of the highly localized heating, the temperature near the filler metal and bond line changes dramatically with distance from the heat source, namely, the highest temperature is restricted to the heat source, from which temperature decreases in filler metal and parent material. Owing to the non-uniform temperature profile and material properties, the shrinkage varies in different regions during the cooling process and, therefore, the highest tensile stress occurs at the welding bond line. The material discontinuity near the interface between filler and base metal results in discontinuous stress profile at that region.

4.2 Hoop residual stress

A stress acting perpendicular to the radius direction is termed a hoop residual stress, denoted $\sigma_{\theta\theta}$ in Fig. 6. Fig. 13 (b) represents the distributions of the hoop residual stress $\sigma_{\theta\theta}$ in both FIB-DIC measurements and FE modelling with optimal interface b. The hoop residual stress develops as a consequence of hoop expansion and shrinkage during the welding process. The highest tensile stress, again, appears near the bond line, followed by a sudden drop and finally becomes compressive as the

distance from the center increases. The hoop stress at the bond line is 580 MPa, approaching the filler metal yield stress. The compressive stresses are formed as a result of weldment self-equilibrium. A sudden drop in hoop stress was observed by FEM near the bond line. The stress discontinuity is due to the mismatch between material properties of the base metal and filler material near the bond line.

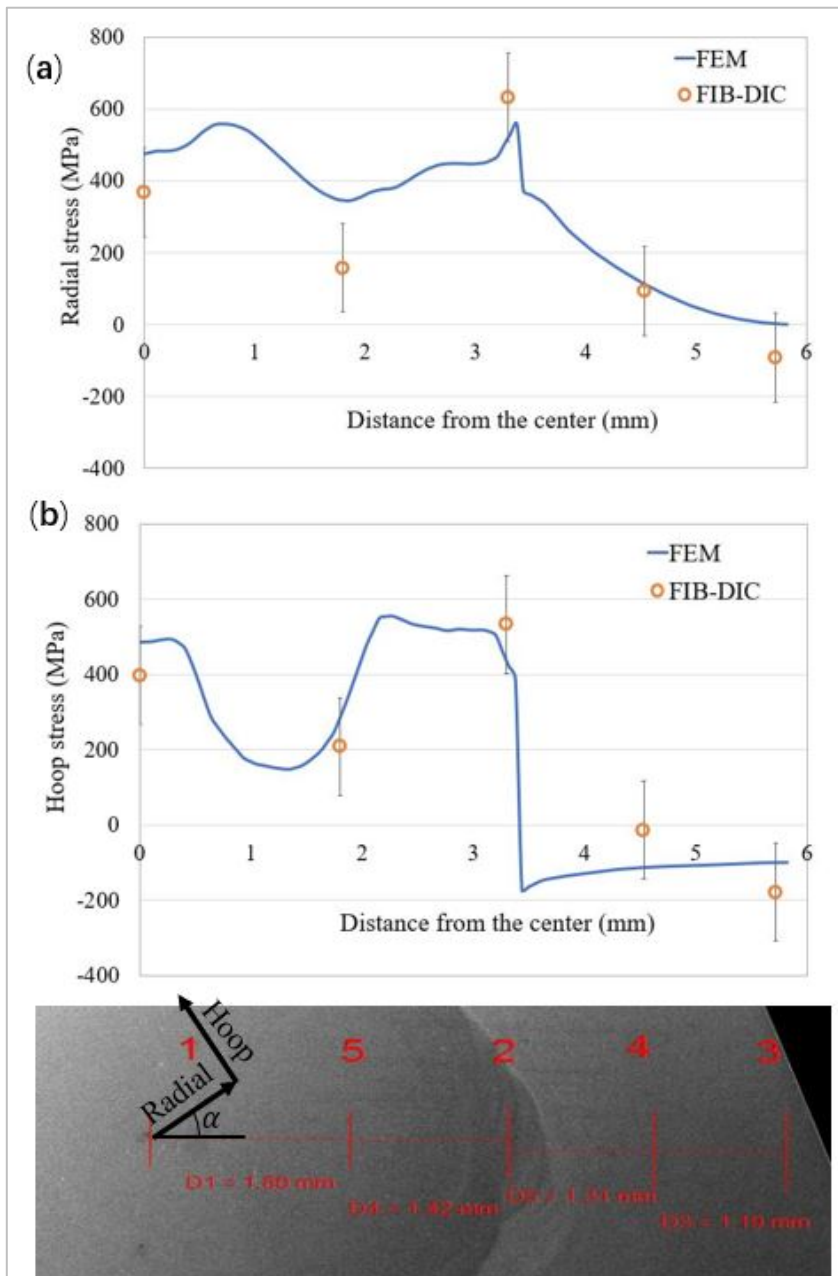


Figure 13. Residual stress distribution obtained from FIB-DIC and FEM simulation with interface b. (error bars

represent a 95% confidence interval). (a) Component of residual stress in the radial direction. (b) Component of residual stress in the hoop direction.

4.3 Discussion

In the present study, it is important to point that highest tensile hoop and radial stress were both observed to occur in the weld line, and their magnitudes approach the yield strength of filler metal. Consequently, these tensile residual stresses increase the effective mean stress under fatigue loading. The presence of sub-surface tensile residual stress is likely to accelerate the initiation and propagation stages of fatigue cracks, while the compressive residual stress near the surface may be beneficial to fatigue life [32,33]. Minimizing the magnitude of the tensile stress clearly provides an opportunity to increase the allowable service stress in this region of the component. PWHT can be performed in order to reduce the tensile residual stress level in welding joint, or alternatively, shot-peening, autofrettage and other surface treatment can introduce beneficial compressive residual stresses near the surface to increase fatigue life.

Whilst this FIB-DIC measurement and FE modelling provide an initial assessment of the overall stress magnitude, it is a well-known fact in residual stress analysis of welds that the largest stresses invariably arise close to the bond line, in the heat affected zone, for the component aligned with the bond. In this case, this line of reasoning would lead to the anticipation of the largest stresses in the hoop direction, close to the interface between the filler metal and parent material. It is important to consider that the residual stress distribution is different in the two TIG welded samples. Local thermal history during welding needs to be measured in order to get a more accurate residual stress simulation.

Given the inherent variability in manual welding processes, it is not surprising that scatter in the measured residual stress levels was observed.

The remaining minor mismatch between experimental measurements and FEM prediction is likely to be due to the use of axisymmetric model and a simplified heat source that limit the precision with which the thermo-mechanical history of deformation can be described, and how closely the residual stress distribution around the weld can be matched. Nevertheless, the wide error bars in experiment data indicate a relatively large uncertainty in the FIB-DIC measurements. It is evident that nearly all the experimental data is within the error bar representing a 95% confidence interval, supporting the proposed heat source model. Therefore, as far as residual stress evaluation is concerned, an good agreement can be achieved between experimental evaluation and simulation using a sequentially coupled thermo-mechanical model.

The simplifications that were made in formulating the model were necessary to enable the calculations to be performed. For example, a full 3D description and simulation of the thermo-mechanical process could have been able to capture finer details of the residual stress distribution. However, this calculation strategy would have required a substantial computational effort, and in any case would require the level of detail in characterisation that cannot be practically realised. Therefore, at this stage of the research it was not deemed reasonable to increase the model complexity any further. Accounting for uncertainties and simplifying assumptions was embedded in our calculation of error propagation. However, further refinements of the numerical and experimental results fidelity can be achieved by accounting for the elastic and plastic anisotropic behaviour. Along with the scatter due

to the variability of the manual welding process, these considerations provide explanations of the very minor discrepancies found between FEM results and experiment data, and also give insights into possible further improvement of the model.

5. Conclusion

In this study, both experimental and sequentially coupled thermo-mechanical analyses were performed to study the residual stress state near manual welding surface along radial and hoop directions. The highest hoop and radial tensile residual stresses were both observed at the boundary surface between the filler metal and base metal, a compressive region was found for hoop stress at the edge of base metal. The magnitude of maximum tensile stress is close to the yield point of filler metal, limiting the allowable service stress of engineering components in service. Such high magnitude of tensile residual stresses is therefore detrimental as concerns the structural integrity of the manufactured object, particularly with the respect of the fatigue life. These evidences lead us to believe that further PWHT, or more in general surface treatment are required to obtain better performance.

According to the microstructure shown in EBSD mapping, the grains in filler metal are narrow and highly elongated in the radial direction with respect to the sample center. This particular grain shape is argued to form because of the steeper temperature gradient during welding process in the radial direction compared to hoop direction. Since the temperature changes dramatically only in radial

direction in current FEM model, the above argument provides a strong support in terms of performing welding simulation using axisymmetric model and a simplified Gaussian heat source. However, it is important to point out that the welding process analysed in this work had been conducted manually, so some variations might be expected from sample to sample. Nevertheless, despite the axisymmetric simplification of the FEM model and variability of results given by the welding operator, the results obtained in this study show a good agreement (experiment vs. simulation), therefore it is possible to confidently say that the underlying residual stress origin has been captured by the model. In turns, this agreement also allows to state that the experimental residual stress profiles are compatible with the geometry and therefore it reinforces the soundness of the findings.

Acknowledgement

This work was supported by Rolls-Royce plc.

Authors contribution:

All authors contributed substantially to the study. J.C.; Wrote the paper, performed experiments and simulation. E.S.; Performed simulation, analyzed data and revised the paper. F.U.; Performed simulation and revised the paper. C.P., Z.W., J.E.; Performed experiments. A.M.K.; Supervised the research and revised the paper.

REFERENCES

- [1] Vacchieri E, Holdsworth SR, Costa A, Poggio E, Riva A, Villari P, et al. Creep – fatigue interaction in two gas turbine Ni based superalloys subjected to service-like conditions. *Mater High Temp* 2014;7:103–10. <https://doi.org/10.1179/0960340914Z.000000000052>.
- [2] Al-Jarba, Fuchs GE. Effect of carbon additions on the as-cast microstructure and defect formation of a single crystal Ni-based superalloy. *Mater Sci Eng A* 2004;373:255–67. <https://doi.org/10.1016/j.msea.2004.01.030>.
- [3] Furtado HC, May I Le. High Temperature Degradation in Power Plants and Refineries. *Mater Res* 2004;7:103–10. <http://dx.doi.org/10.1590/S1516-14392004000100015>.
- [4] Salvati E, Korsunsky AM. An analysis of macro- and micro-scale residual stresses of Type I, II and III using FIB-DIC micro-ring-core milling and crystal plasticity FE modelling. *Int J Plast* 2017;98:123–38. <https://doi.org/10.1016/j.ijplas.2017.07.004>.
- [5] Withers PJ, Bhadeshia HKDH, Withers PJ, Bhadeshia HKDH. Residual stress. Part 2 – Nature and origins. *Mater Sci Technol* 2001;17:366–75. <https://doi.org/10.1179/026708301101510087>.
- [6] Radaj D. Heat effects of welding: temperature field, residual stress, distortion. Springer Science & Business Media; 2012.
- [7] Woo W, Em V, Hubbard CR, Lee H, Soo K. Residual stress determination in a dissimilar weld overlay pipe by neutron diffraction. *Mater Sci Eng A* 2011;528:8021–7. <https://doi.org/10.1016/j.msea.2011.07.059>.
- [8] Korsunsky AM, Sebastiani M, Bemporad E. Residual stress evaluation at the micrometer scale: Analysis of thin coatings by FIB milling and digital image correlation. *Surf Coat Technol* 2010;205:2393–403. <https://doi.org/10.1016/j.surfcoat.2010.09.033>.
- [9] Korsunsky AM, Sebastiani M, Bemporad E. Focused ion beam ring drilling for residual stress evaluation. *Mater Lett* 2009;63:1961–3. <https://doi.org/10.1016/j.matlet.2009.06.020>.
- [10] Abadías G, Chason E, Keckes J, Sebastiani M, Thompson GB, Barthel E, et al. Stress in thin films and coatings: Current status, challenges, and prospects. *J Vac Sci Technol A* 2018;36. <https://doi.org/10.1116/1.5011790>.
- [11] Guo Y, Abdolvand H, Britton TB, Wilkinson AJ. Growth of $\{11\bar{2}2\}$ twins in titanium: A combined experimental and modelling investigation of the local state of deformation. *Acta Mater* 2017;126:221–35. <https://doi.org/10.1016/j.actamat.2016.12.066>.
- [12] Kartal ME, Kiwanuka R, Dunne FPE. Determination of sub-surface stresses at inclusions in single crystal superalloy using HR-EBSD, crystal plasticity and inverse eigenstrain analysis. *Int J Solids Struct* 2015;67–68:27–39. <https://doi.org/10.1016/j.ijsolstr.2015.02.023>.

- [13] Jiang J, Britton T Ben, Wilkinson AJ. The orientation and strain dependence of dislocation structure evolution in monotonically deformed polycrystalline copper. *Int J Plast* 2015;69:102–17. <https://doi.org/10.1016/j.ijplas.2015.02.005>.
- [14] Wan VVC, Cuddihy MA, Jiang J, Maclachlan DW, Dunne FPE. An HR-EBSD and computational crystal plasticity investigation of microstructural stress distributions and fatigue hotspots in polycrystalline copper. *Acta Mater* 2016;115:45–57. <https://doi.org/10.1016/j.actamat.2016.05.033>.
- [15] Lunt AJG, Korsunsky AM. A review of micro-scale focused ion beam milling and digital image correlation analysis for residual stress evaluation and error estimation. *Surf Coat Technol* 2015;283:373–88. <https://doi.org/10.1016/j.surfcoat.2015.10.049>.
- [16] Belnoue JP, Jun T, Hofmann F, Abbey B, Korsunsky AM. Evaluation of the overload effect on fatigue crack growth with the help of synchrotron XRD strain mapping. *Eng Fract Mech* 2010;77:3216–26. <https://doi.org/10.1016/j.engfracmech.2010.08.018>.
- [17] Salvati E, Romano-brandt L, Mughal MZ, Sebastiani M, Korsunsky AM. Journal of the Mechanics and Physics of Solids Generalised residual stress depth profiling at the nanoscale using focused ion beam milling. *J Mech Phys Solids* 2019;125:488–501. <https://doi.org/10.1016/j.jmps.2019.01.007>.
- [18] Joris E, Brandt R, Zhang H, Everaerts J, Salvati E, Uzun F, et al. Separating macro- (Type I) and micro- (Type II + III) residual stresses by ring-core FIB-DIC milling and eigenstrain modelling of a plastically bent titanium alloy bar. *Acta Mater* 2018;156:43–51. <https://doi.org/10.1016/j.actamat.2018.06.035>.
- [19] Harris K, Erickson GL, Schwer RE, Frasier DJ, Whetstone JR. Process and Alloy Optimization for CMSX-4 Superalloy Single Crystal Airfoil. In: *Cost Conference Liege, Proc. Part II* 1990.
- [20] Sengupta A, Putatunda SK, Bartosiewicz L, Hangas J, Peputapeck M, Alberts EE. Tensile Behavior of a New Single-Crystal Nickel-Based Superalloy (CMSX-4) at Room and Elevated Temperatures. *J Mater Eng Perform* 1994;3:73–81. <https://doi.org/10.1007/BF02654502>.
- [21] Baicheng Z, Xiaohua L, Jiaming B, Junfeng G, Pan W, Chen-nan S, et al. Study of selective laser melting (SLM) Inconel 718 part surface improvement by electrochemical polishing. *Mater Des* 2017;116:531–7. <https://doi.org/10.1016/j.matdes.2016.11.103>.
- [22] Everaerts, J., Salvati, E. and Korsunsky, A.M. Nanoscale depth profiling of residual stresses due to fine surface finishing. *Adv Mater Inter*, 2019;1900947. <https://doi.org/10.1002/admi.201900947>.
- [23] Salvati E, Connor SO, Sui T, Nowell D, Korsunsky AM. A study of overload effect on fatigue crack propagation using EBSD, FIB – DIC and FEM methods. *Eng Fract Mech* 2016;167:210–23. <https://doi.org/10.1016/j.engfracmech.2016.04.034>.
- [24] Salvati E, Sui T, Korsunsky AM. Uncertainty quantification of residual stress evaluation by the FIB – DIC ring-core method due to elastic anisotropy effects. *Int J Solids Struct* 2016;87:61–9. <https://doi.org/10.1016/j.ijsolstr.2016.02.031>.
- [25] Salvati E, Korsunsky AM. Micro-scale measurement & FEM modelling of residual stresses in AA6082- T6 Al alloy generated by wire EDM cutting. *J Mater Process Tech* 2020;275:116373. <https://doi.org/10.1016/j.jmatprotec.2019.116373>.
- [26] Lu, M, Kou, S. Power and current distribution in Gas Tungsten Arcs. *Weld. J.* 1988;67: 29-33.

- [27] Mousavi SAAA, Miresmaeili R. Experimental and numerical analyses of residual stress distributions in TIG welding process for 304L stainless steel 2008;8:383–94. <https://doi.org/10.1016/j.jmatprotec.2008.01.015>.
- [28] ABAQUS, V. (2007). *ABAQUS standard user's manual: Version 6.7*.
- [29] Siebo D. Temperature dependence of the elastic moduli of the nickel-base superalloy CMSX-4 and its isolated phases. Mater Sci Eng A 2001;298:26–33. [https://doi.org/10.1016/S0921-5093\(00\)01318-6](https://doi.org/10.1016/S0921-5093(00)01318-6).
- [30] Hightechalloys.de. Elgiloy® The Co-Cr-Ni Alloy. [online] Available at: http://hightechalloys.de/pdf/Elgiloy_Flyer.pdf. [Accessed 4 July. 2019].
- [31] Matweb.com. Elgiloy® Co-Cr-Ni Alloy, Wire. [online] Available at: <http://www.matweb.com/search/datasheet.aspx?MatGUID=9bd90091755740648e2afa5cdb9fb09b>. [Accessed 4 July. 2019].
- [32] Webster GA, Ezeilo AN. Residual stress distributions and their influence on fatigue lifetimes. Int J Fatigue 2001;23:375–83. [https://doi.org/10.1016/S0142-1123\(01\)00133-5](https://doi.org/10.1016/S0142-1123(01)00133-5).
- [33] James MN. Residual stresses and fatigue performance. Eng Fail Anal 2007;14:384–95. <https://doi.org/10.1016/j.engfailanal.2006.02.011>.

Figure Caption

Figure 1. The overall geometry of the welded specimen with arrows showing the weld infill (left), and a cross-section view through the weldment (right).

Figure 2. Secondary electron images showing the microstructure of the welded specimen at different locations: (a) The interface between welding metal Polymet 972 and unaffected base metal CMSX-4. (b) A close-up image of the interface. (c) The microstructure of single crystal base metal. (d) The microstructure of welding area.

Figure 3. (a) SEM image showing the texture analysis area. (b) Inverse pole figure map for a quarter of the sample (with respect to the hoop direction).

Figure 4. The FIB-DIC measurement positions in the sample surface.

Figure 5. (a) An illustration of the FIB milling process. (b) A sample showing strain relief in two referent directions. D is the micropillar diameter and h is the milling depth.

Figure 6. Radial stress (σ_{rr}) and hoop stress ($\sigma_{\theta\theta}$) obtained from FIB-DIC measurements with error bars at 95% confidence. The dash guideline curve shows the averaged radial stress with respect to distance from center, while solid line represents the trend of averaged hoop stress.

Figure 7. (a) The geometry of the sample. (b) The corresponding axisymmetric model with 3 different interface lines. (c) The refined mesh with interface b. The radial direction is along the x coordinate, while the hoop direction

is perpendicular to the x-y plane.

Figure 8. Temperature dependent mechanical properties.

Figure 9. (a) The proposed route of heat source from the center to the edge. (b) An illustration of simplified heat source in axisymmetric model. (c) The heating parameters used in this simulation.

Figure 10. The distribution of radial stress (left) and hoop stress (right) right after welding in the model with optimal interface b.

Figure 11. Three stress components distribution before ((a), (c), (e)) and after ((b), (d), (f)) material removal with optimal interface b.

Figure 12. Radial (top) and hoop (bottom) residual stress obtained from FEM near the top surface after cutting with three interfaces. Path $A-A'$, $B-B'$ and $C-C'$ indicate the position of interface a, b and c, respectively.

Figure 13. Residual stress distribution obtained from FIB-DIC and FEM simulation with interface b. (error bars represent a 95% confidence interval). (a) Component of residual stress in the radial direction. (b) Component of residual stress in the hoop direction.